Corrosion Behavior of Titania Films Coated by Liquid-Phase Deposition on AISI304 Stainless Steel Substrates

Yongwei Cai
Dept. of Chemical Engineering, School of Chemical Engineering and Technology,
Tianjin University, Tianjin 300072, China

Mingyan Liu
Dept. of Chemical Engineering, School of Chemical Engineering and Technology,
Tianjin University, Tianjin 300072, China

State Key Laboratory of Chemical Engineering, Tianjin 300072, China

DOI 10.1002/aic.12701

Fouling deposition and localized corrosion on the heat-transfer surfaces of the stainless steel equipments often simultaneously exist, which can introduce additional thermal resistance to heat-transfer and damage heat-transfer surfaces. It is a good anticorrosion way to coat a barrier layer of certain materials on the metal surface. In this article, the TiO_2 coatings with nanoscale thicknesses were obtained by liquid-phase deposition method on the substrates of AISI304 stainless steel (ASS). The coating thickness, surface roughness, surface morphology, crystal phase, and chemical element were characterized with the film thickness measuring instrument, roughmeter, atomic force microscopy, field emission scanning electron microscopy, X-ray diffraction, and energy-dispersive X-ray spectroscopy analyzer, respectively. Corrosion behavior of the TiO_2 coatings was evaluated by potentiodynamic polarization, cyclic voltammograms scanning, and electrochemical impedance spectroscopy tests with the mixed corrosion solution composed of 3.5 wt. % NaCl and 0.05 M NaOH. It is shown that the TiO_2 coating is composed of the nanoparticles with smooth, crack-free, dense, and uniform surface topography; the roughness of coating surface increases slightly compared with that of the polished ASS substrate. The anatase-phase TiO_2 coatings are obtained when sintering temperature being varied from 573.15 to 923.15 K and exhibit better anticorrosion behavior compared with ASS surfaces. The corrosion current density decreases and the polarization resistance increases with the increase of the coating thickness. The corrosion resistance of the TiO_2 coatings deteriorates with the increase of the corrosion time. The capacitance and the resistance of the corrosion product layer between the interface of the ASS substrate and the TiO_2 coating are found after the corrosion time of 240 h. A corrosion model was introduced, and a possible new explanation on the anticorrosion mechanisms of the TiO_2 coating was also analyzed. The corrosion mechanism of the TiO_2 coating might comply with the multistage corrosion process. © 2011 American Institute of Chemical Engineers *AIChE J,* 58: 1907–1920, 2012

Keywords: coating, corrosion, titania, liquid-phase deposition, electrochemical impedance spectroscopy, Tafel curves, cyclic voltammetry, AISI304 stainless steel

Introduction

Fouling deposition and corrosion on heat-transfer surfaces of metal materials often exist simultaneously.[1,2] Therefore, investigations on the anticorrosion characteristics of the heat-transfer surfaces are as important as those on the antifouling properties. Stainless steel materials are susceptible to localized corrosion[3] in the solution with dissolved oxygen and the chloride or other aggressive ions[4] although they are famous for their good corrosion resistance. The corrosion of stainless steel damages the heat-transfer surface. In addition, the corrosion products (i.e., in situ corrosion fouling[5]) formed on the heat-transfer surface can introduce a thermal resistance to heat transfer, and provide nooks and crannies in which the precipitation of calcium carbonate or calcium sulfate fouling is promoted. So, the corrosion of the stainless steel has attracted much attention from heat-transfer domains.

The surface coating technology is an alternative to corrosion protection of stainless steel due to the formation of barrier over the metal surface to block the interaction between metal substrate and electrochemical environment.[5] Titania coating has been paid widespread attention due to its unique photocatalytic properties[6] as well as its antifouling functions.[7–9] The TiO_2 coatings have low electronic conductance, good insulating properties, and low anodic dissolution rate, so it was also widely used for protection against metal corrosion.[10–13]

Correspondence concerning this article should be addressed to M. Y. Liu at myliu@tju.edu.cn.

Titanium dioxide coatings have been prepared by reactive pulse magnetron sputtering,[6] cathodic vacuum arc deposition,[14] chemical vapor deposition (CVD),[15,16] self-assembled monolayers (SAMs),[17] sol–gel[18], and liquid-phase deposition (LPD) methods.[7,9,19,20] The LPD method was reported earlier for depositing SiO_2[21] coatings and subsequently for TiO_2 coatings[20] on a variety of substrates, such as glass,[22,23] mica,[23] carbon fiber,[24] and metals[25] near room temperature. The LPD method has many advantages. It requires simple equipment and lower deposition temperature, and it is applicable to substrates that cannot withstand high temperature as well as is able to deposit on the large size and complex shape substrates. Generally, the TiO_2 coatings can be heated at different temperature to obtain various crystal forms.[26,27]

The electrochemical method to evaluate the anticorrosion property of the TiO_2 coatings was widely used in the published articles. Głuzek et al.[28] studied the corrosion behavior of the TiO_2 coating on 316L stainless steel by the plasma-assisted CVD method in Ringer solution using the impedance spectroscopy and polarization examinations. The results show that the TiO_2 coating increases the resistivity of the 316L type stainless steel to pitting corrosion and general corrosion. Szalkowska et al.[10] obtained the TiO_2 coating by sol–gel technique on the AISI403 type steel surface to examine the corrosion protecting properties with polarization and impedance measurements in the solution of 0.5 mol L^{-1} Na_2SO_4 acidified down to pH of 3. The results demonstrate that the TiO_2 coating inhibits both the cathodic and anodic corrosion processes, and the corrosion rate is by two orders of magnitude lower than that of the bare steel surface. Shen et al.[11] prepared the TiO_2 nanoparticle coating on 316L stainless steel using sol–gel method and used the Tafel polarization curves and electrochemical impedance spectroscopy (EIS) to measure the anticorrosion performance of the TiO_2 coatings in 0.5 mol L^{-1} NaCl solution with pH of 4.6. The results indicate that the TiO_2 nanoparticle coating exhibits an excellent corrosion resistance due to ceramic protective barrier on metal surface. Hu et al.[25] prepared the TiO_2 coating for AZ31 magnesium alloy by LPD method and evaluated the corrosion protection performance in 3.5 wt. % NaCl solution with Tafel polarization technique. The results display that the anatase-type phase TiO_2 coating shows evident corrosion resistance and with the increase of the annealing temperature and prolongation of annealing time, the anticorrosion property is improved. However, the coating thickness is about 1.0×10^{-5} m and the annealed temperature is $\leq$653.15 K. Such a thick coating is easily cracked and desquamated when it is dried and annealed. Meanwhile, the coating might have high-additional thermal resistance when it is coated onto the heat-transfer surface. The durability of the coating in the corrosion solution with the increase of the corrosion time and the corrosion mechanism of the coating need to be explored. Zeng et al.[19] prepared the anatase-type TiO_2 coating on the 304 stainless steel substrate by the LPD method with film thickness of greater than 4.5×10^{-7} m under annealing temperature of 673.15 K. The coating is thick and cracked. Recently, Padhy et al.[5] studied the corrosion performance of the sputter deposited TiO_2 coating on the 304L type stainless steel in the oxidizing medium of 1 mol L^{-1} and 8 mol L^{-1} nitric acid. Their results show an increase in the corrosion resistance in the test solutions and a surface dissolution at higher concentrations of nitric acid for TiO_2-coated specimens. Wang and Liu[9] qualitatively carried out the dipping experiments of the amorphous TiO_2-coated surface on the red copper substrate in the corrosion media at room temperature. The experimental results indicate that the TiO_2 coating can resist corrosion until 900 h (1 h = 3600 s) in 25 wt. % NaCl solution, and the coating shows better anticorrosion behavior than the copper metal in 30 wt. % NaOH solution. However, the coating is easily corroded in 30 wt. % HCl solution. The corrosion mechanism needs further extensive and quantitative investigations.

In corrosion studies, the 316L stainless steel as well as other more costly metal alloy was often selected as the substrates. It is known that the austenitic AISI304 stainless steel (ASS) is the major constructional material for the fabrication of vessels, pipes, tanks, and equipments in heat-transfer field because of its relatively low price. However, little systematical and qualitative work is available in the literature on the corrosion performance of the anatase phase of the TiO_2 coatings with nanoscale thickness prepared by LPD method on the ASS substrates.

In this study, the uniform anatase-phase TiO_2 nanoparticle coatings on the ASS substrates were fabricated by LPD method, and their corrosion behavior was investigated. The crystallinity and nanostructural features of the TiO_2 coating were characterized by X-ray diffraction (XRD) and field emission scanning electron microscopy (FE-SEM), respectively. The elemental distribution of the TiO_2 coatings was analyzed by the energy-dispersive X-ray spectroscopy (EDS) analyzer. The surface roughness of the coatings was measured by the roughmeter and atomic force microscopy (AFM). The coating thickness was gauged with the measurement instrument of thin film thickness. The potentiodynamic (Tafel) polarization (PP), cyclic voltammetry (CV), and EIS technique were used to measure the corrosion performance of the TiO_2 coating in 3.5 wt. % NaCl corrosion solution, and 0.05 mol L^{-1} NaOH was added in the solution to enhance the corrosion process.[29,30] Meanwhile, the morphology of the specimen surface after corrosion was observed by FE-SEM, and a corrosion model was proposed to help analyze the corrosion mechanism of the TiO_2 coating surface.

Methods of TiO_2 Coating Preparation, Characterization, and Tests of Corrosion Behavior

Preparation of TiO_2 coatings

Hexafluorotitanate ammonium ($(NH_4)_2TiF_6$, Shanghai SSS Reagent, China) and boric acid (H_3BO_3, Tianjin Kemiou Chemical Reagent, China) were dissolved, respectively, in deionized water. $(NH_4)_2TiF_6$ and H_3BO_3 solutions were mixed at various compositions and used as the solution for deposition of the TiO_2 coatings. The ASS substrate was grinded with different size of SiC abrasive papers and polished with the polishing machine (MINITOR, Japan) smeared with the polishing paste. Then, the substrates were degreased and washed ultrasonically with acetone and ethanol. After that, they were rinsed by deionized water. The treated substrates were immersed into the deposition solution for coating. The temperature of the solution was kept at a certain temperature. After the appropriate reaction time, the sample was taken out from the deposition solution and gently rinsed with deionized water and dried at room temperature. These samples were calcined in the resistance furnace (KSXQ-6-14, Yixing Feida Electric Resistance Furnace,

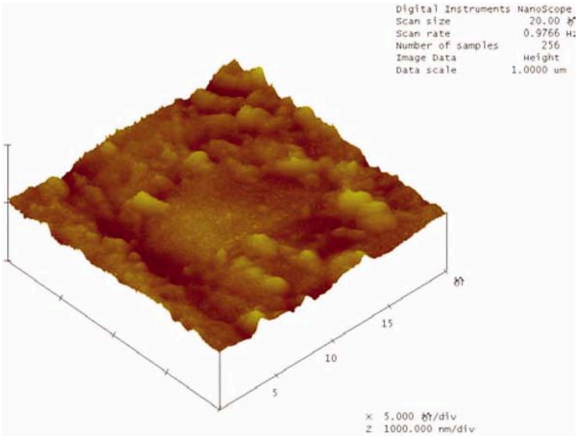

Figure 1. Three-dimensional AFM image of the TiO_2 coating surface.

[Color figure can be viewed in the online issue, which is available at wileyonlinelibrary.com.]

China) at various temperatures with fixed heating rate under nitrogen flow.

For the hydrolysis (ligand-exchange) reaction of $[TiF_6]^{2-}$ ion in aqueous solution, the following equilibrium scheme has been proposed by Schmitt et al.[31]

$$[TiF_6]^{2-} + nH_2O \rightleftharpoons [TiF_{6-n}(OH)_n]^{2-} + nHF \qquad (1)$$

H_3BO_3 was added into the treatment solution as F^- scavenger. H_3BO_3 easily reacts with F^- ion and forms more stable complex as the following reaction equation.[32]

$$H_3BO_3 + 4HF \rightleftharpoons HBF_4 + 3H_2O \qquad (2)$$

Consequently, titanium dioxide coatings are formed on the substrates of $[Ti(OH)_6]^{2-}$ species generated by the hydrolysis reaction of $[TiF_6]^{2-}$.[20,33]

Thickness measurement of coatings

The thickness of TiO_2 coating was gauged with the film thickness measuring instrument (SGC-10, Tianjin Gangdong Scientific and Technical Development, China), which uses a noncontact optical evaluation measurement technology from the New Span Opto-Technology.[34] It is worth noting that the film and the substrate surface should have smaller roughness and only the transparent or translucent film is available for measurement of the film parameters. The film thickness and its optical constants (refractive index and extinction coefficient) are measured by fitting the interferometry spectrum formed by two beams of the reflected light, that one is from the outer surface of the film, and the other is from the interface between the film and the substrate. When the shape of the measurement curve is similar to that of the fitting curve, the measurement result of the coating thickness is accurate.

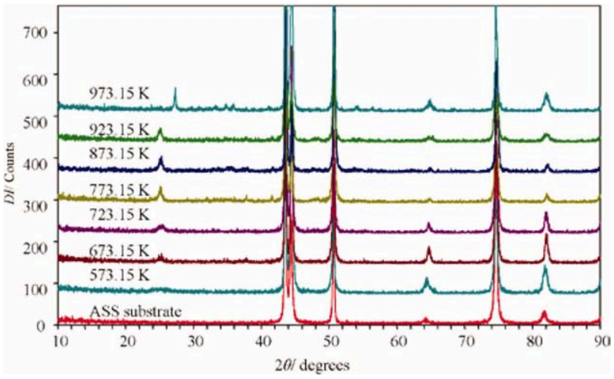

Figure 2. Effect of the annealing temperature on the crystalline phases of the TiO_2 coatings.

[Color figure can be viewed in the online issue, which is available at wileyonlinelibrary.com.]

Surface roughness, topography measurements and chemical element analyses

The surface roughness was measured with the roughmeter (JB-8C, Guangzhou Guangjing Precision Instrument, China). The instrument has a natural diamond skid type stylus with tip radius of 5×10^{-6} m and tip angle of 90°. The stylus links with free lead head type sensors, which change the vertical displacement of the stylus into an electrical signal.

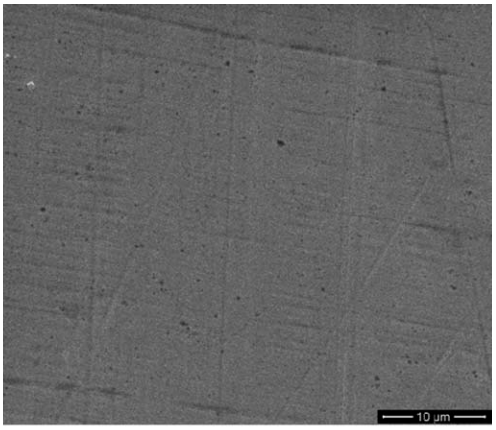

(a) FE-SEM (5000X)

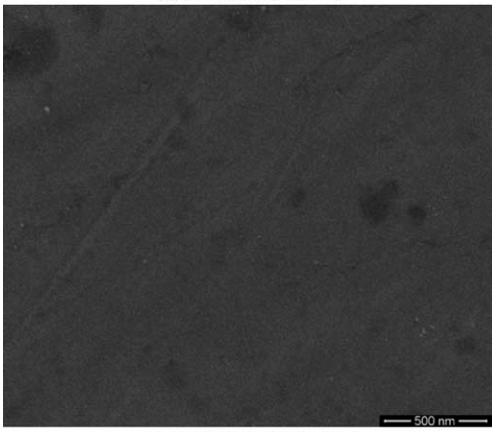

(b) FE-SEM (100000X)

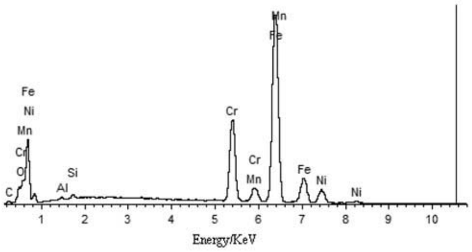

(c) EDS mapping image

Figure 3. Plan view FE-SEM images of the ASS.

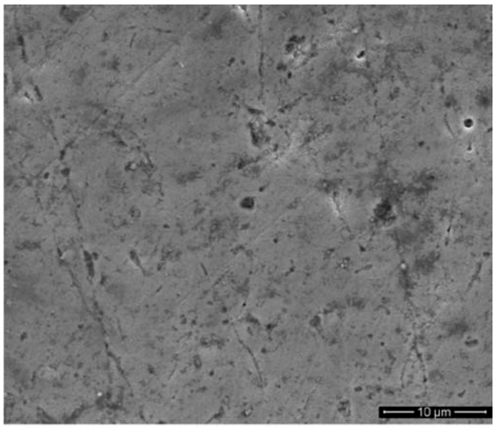

(a) FE-SEM (5000X)

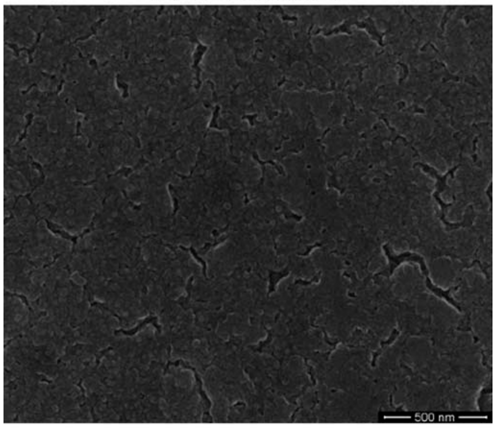

(b) FE-SEM (100000X)

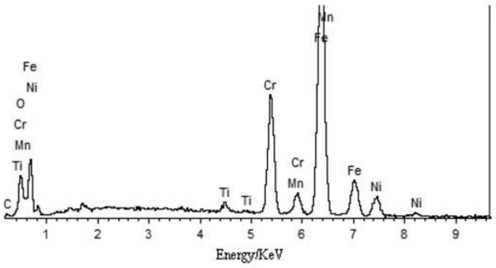

(c) EDS mapping image

Figure 4. Plan view FE-SEM images of the TiO_2 coating with thickness of $79.1 \pm 0.5 \times 10^{-9}$ m annealed at 873.15 K.

The vertical and horizontal displacement signals of the stylus can be obtained and converted to datum graphs. The parameters of cut-off wavelength were set to 8×10^{-4} m, scan length 4.0×10^{-3} m, and scan speed 3.2×10^{-4} m s^{-1}. To ensure the accuracy of the measurement results, no less than five different locations of the same sample surface were selected randomly, and the average of the measurement results was calculated. The maximum height of profile R_z is sum of the height of the largest profile peak and the largest profile valley depth within one sampling length l_r.[35] The arithmetical mean deviation R_a is defined as the arithmetic mean of the ordinate $Z(x)$ absolute value within one l_r.[35] The root mean square deviation R_q is defined as the root mean square value of the ordinate $Z(x)$ within one l_r.[35]

The surface topography of the coating was checked by AFM (D3100M MMAFM/STM, USA). The AFM images were taken in a tapping mode with a Si_3N_4 tip. AFM topographic images were recorded over scan areas of 4×10^{-4} m^2, each with a resolution of 256 ×256 data points, and the scan rate is 0.9766 Hz.

The morphology and the elemental distribution of the TiO_2 coatings were analyzed by the FE-SEM (Nanosem 430, FEI, USA) coupled with EDS analyzer.

Confirmations of crystal patterns of TiO_2 coatings

The crystallinity of the heat-treated TiO_2 thin coatings was analyzed with XRD (Tokyo Rigaku D/max 2500v/pc, Japan) using $CuK_{\alpha 1}$ (4.0×10^4 V, 0.2 A) radiation and a graphite monochrometer for the diffracted beam. The 2θ values were scanned from 10 to 90°. The step width was 0.02°, and the sample time was 0.15 s.

Electrochemical tests

Three electrochemical analysis methods, PP (Tafel curves), CV, and EIS measurements were performed using

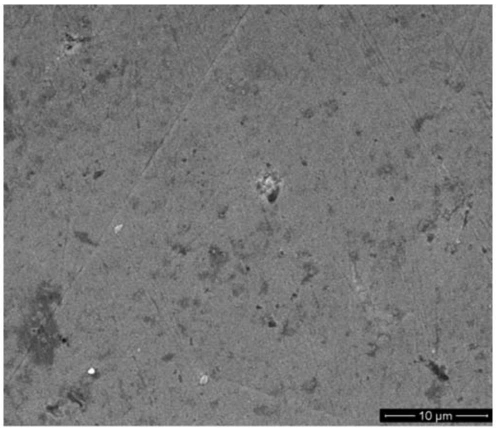

(a) FE-SEM (5000X)

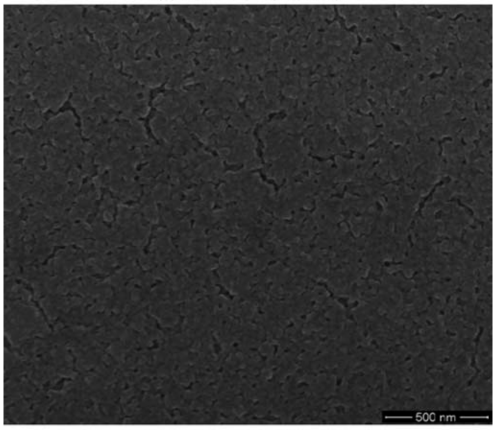

(b) FE-SEM (100000X)

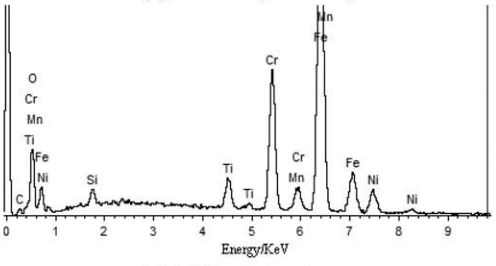

(c) EDS mapping image

Figure 5. Plan view FE-SEM images of the TiO_2 coating with thickness of $228.5 \pm 0.9 \times 10^{-9}$ m annealed at 873.15 K.

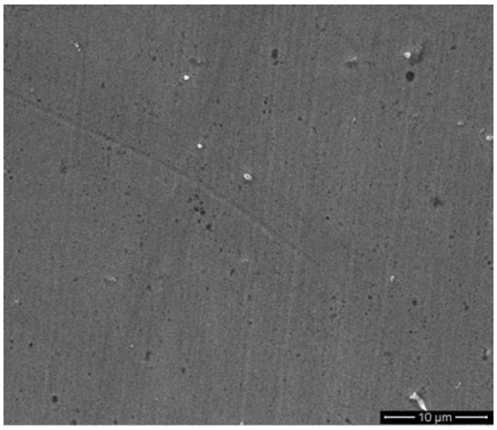

(a) FE-SEM (5000X)

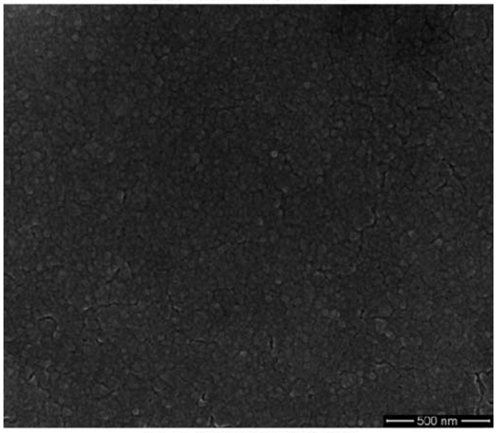

(b) FE-SEM (100000X)

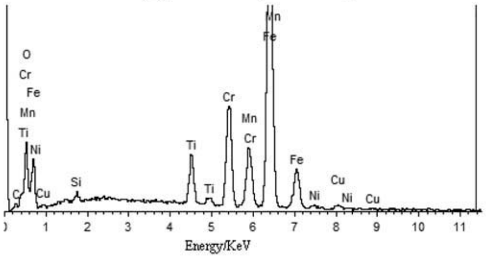

(c) EDS mapping image

Figure 6. Plan view FE-SEM images of the TiO_2 coating with thickness of $288.9 \pm 0.8 \times 10^{-9}$ m annealed at 873.15 K.

computer-controlled potentiostat (PAR273A, Princeton Applied Research), and the associated PowerSuite package was used for total control of the experiments, data acquisition, and treatment. A three-electrode cell configuration was used for the impedance measurements. A saturated calomel electrode (SCE) was used as reference and a spiral platinum wire as auxiliary electrode. The coating specimen serves as the working electrode. The distance between the reference electrode and the working electrode was kept same for all the tests. All the electrochemical tests were performed in the corrosion medium composed of 3.5 wt. % NaCl and 0.05 mol L^{-1} NaOH under free air condition at constant temperature (295.15 K). The pH value of the mixed corrosion solution is 13.43, which was measured by the portable pH meter (PHB-4, Shanghai Precision Scientific Instrument, China). The solutions were neither agitated nor deoxygenated during the experiments. The specimens were embedded in the mixture of epoxy resin and polyamide resin, with the volume ratio of 2:1, and exposed one 2.25×10^{-4} m^2 coating surface, then solidified for 4 h in the digital display blast drying oven with stainless inner container (101-3BS, Longkou Furnace Manufacturer, China). Before the specimens being immersed into the corrosion solution, the coating surface was cleaned with absolute ethyl alcohol and deionized water.[36] Before testing, the samples were previously soaked in the corrosion solution for 10 min to establish the steady state potential.[36] The electrolytic cell was packed into the modified grounded microwave oven without power, which acts as a Faraday cage during each electrochemical test to shield the outside electromagnetic interference. Repeatability was checked by making two measurements for one sample. The spectra were

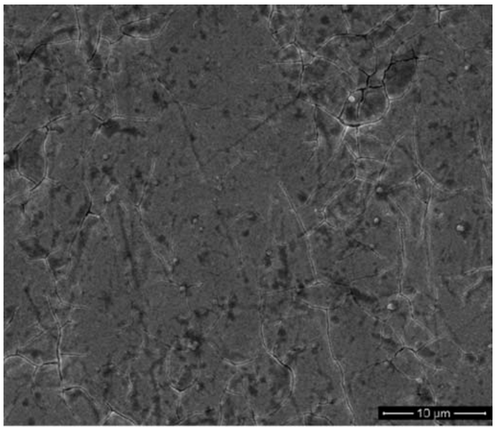

(a) FE-SEM (5000X)

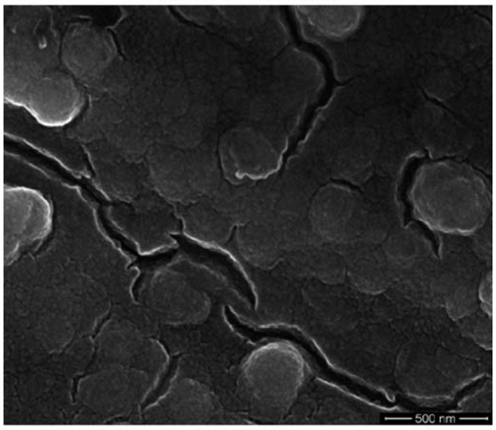

(b) FE-SEM (100000X)

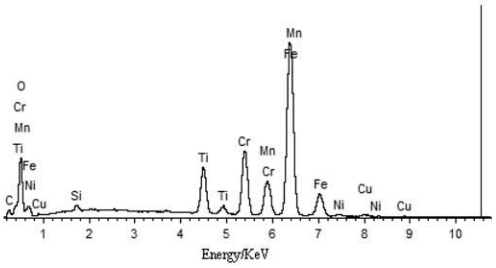

(c) EDS mapping image

Figure 7. Plan view FE-SEM images of the TiO_2 coating with thickness of $326.5 \pm 1.0 \times 10^{-9}$ m annealed at 873.15 K.

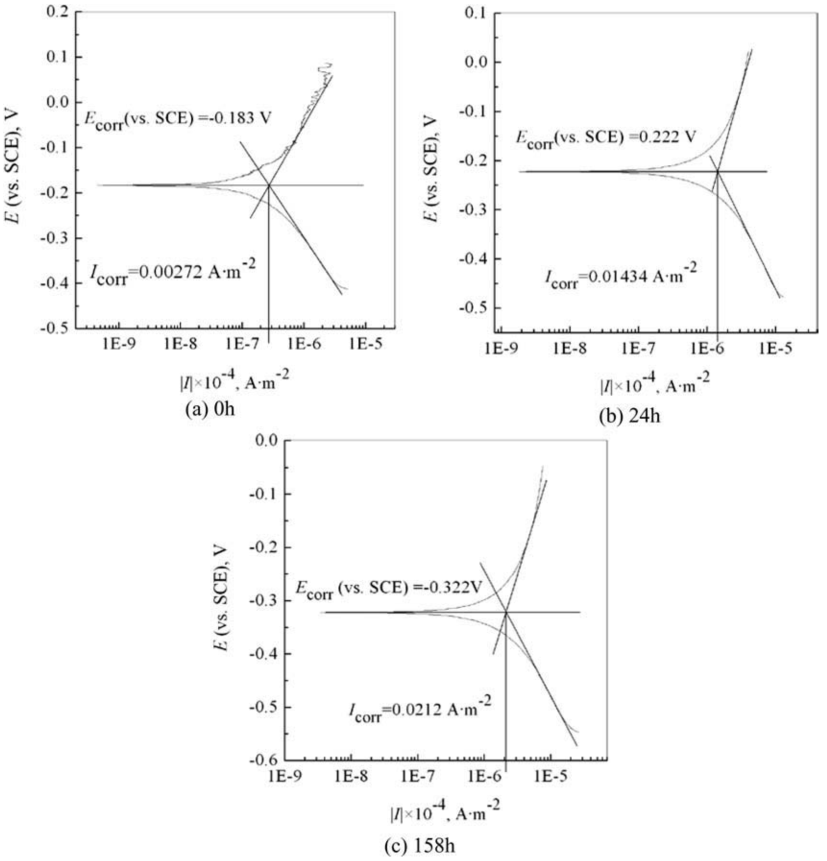

(a) 0h

(b) 24h

(c) 158h

Figure 8. Determination of E_{corr} (vs. SCE) and I_{corr} by Tafel's extrapolation method.

(a) 0 h; (b) 24 h; (c) 158 h.

almost identical, it can be concluded that the measuring systems did not change during the electrochemical tests.

Two electrical equivalent circuits (ECs) were introduced to analyze the impedance data. The constant phase element (CPE), Q, was used to replace the capacitance, because it has hardly pure capacitance in real electrochemical process.[37] The CPE is expressed in the form of admittance as,[38]

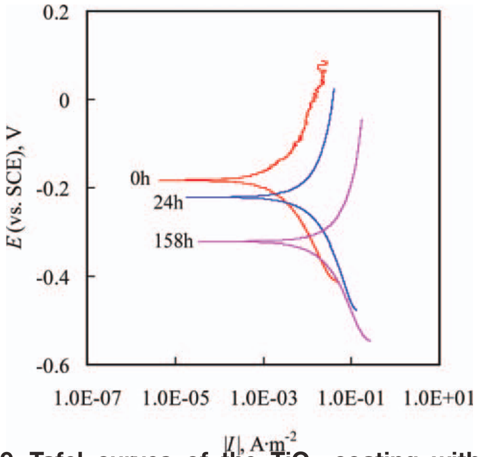

Figure 9. Tafel curves of the TiO_2 coating with thickness of 228.5 ± 0.9 × 10^{-9} m at different corrosion time.

[Color figure can be viewed in the online issue, which is available at wileyonlinelibrary.com.]

$$Y(\omega) = Y_0(j\omega)^n \tag{3}$$

where $j = \sqrt{-1}$. n relates to a non-uniform current distribution due to surface roughness or inhomogeneity.[39] If $n = 1$, CPE is an idea capacitor. If $n = 0$, CPE is a resistor.[10]

The software program, ZSimpWin 3.10, was used to fit the impedance data with the basis of an EC. The program is based on nonlinear least squares, which is available to the simulation of a multivariable function.[38]

Results and Discussion

Coating characterization

Surface Roughness and Topography of TiO_2 Coatings. The untreated surface has a maximum surface roughness with R_a of 3.6 ± 0.2 × 10^{-6} m and R_z of 224.7 ± 2.22 × 10^{-6} m. However, the surface roughness of the polished ASS substrate decreased significantly with R_a of 1.9 ± 0.1 × 10^{-8} m and R_z of 4.4 ± 0.2 × 10^{-5} m. When the

Table 1. Different Electrochemical Parameters Obtained by Tafel Extrapolation

Corrosion Time (h)	E_{corr} (vs. SCE; V)	I_{corr} (A m^{-2})	β_a (V dec^{-1})	β_c (V dec^{-1})	R_p (Ω m^2)
0	−0.183	0.00272	0.237	0.204	17.519
24	−0.222	0.0143	0.496	0.252	5.066
158	−0.322	0.0212	0.408	0.236	3.061

The data are normalized by apparent surface area.

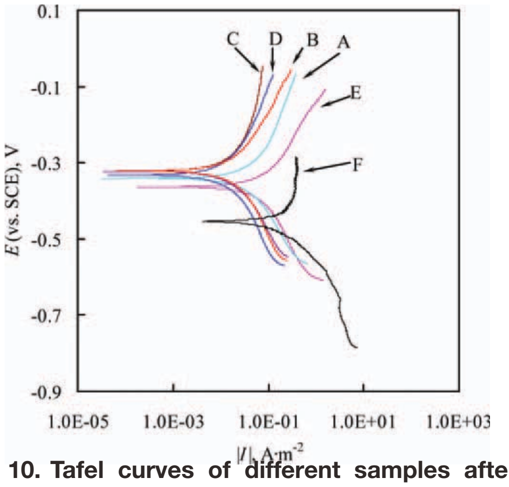

Figure 10. Tafel curves of different samples after the corrosion time of 158 h.

A-79.1 ± 0.5 × 10^{-9} m; B-134.7 ± 0.7 × 10^{-9} m; C-228.5 ± 0.9 × 10^{-9} m; D-288.9 ± 0.8 × 10^{-9} m; E-326.5 ± 1.0 × 10^{-9} m; F-ASS. [Color figure can be viewed in the online issue, which is available at wileyonlinelibrary.com.]

TiO_2 nanoparticles were deposited on the ASS substrate, the roughness is increased ($Ra = 3.7 \pm 0.3 \times 10^{-8}$ m and $R_z = 7.2 \pm 0.8 \times 10^{-7}$ m).

Figure 1 presents a typical surface topography image of the TiO_2 coatings with three-dimensional AFM measurement. The TiO_2 coating consists of many particle peaks and valleys, which distribute randomly on the surface. The values of R_a, R_q, and R_z are 3.6 × 10^{-8} m, 4.6 × 10^{-8} m, and 3.7 × 10^{-7} m, respectively.

Coating Crystal Structure Confirmation. Figure 2 shows the XRD patterns of coatings calcined at different temperatures in nitrogen atmosphere. The amorphous TiO_2 was obtained at temperature of 573.15 K. At 673.15 K, the reflection characteristic peak, 2θ, at 25.28° belongs to the (101) face of the anatase-phase crystal according to JCPDS PDF card 21-1272. However, the width of the diffraction peak shows wider, which indicates the formation of fine crystallites in the coating. From 673.15 to 923.15 K, the peak intensity of anatase phase increases and the peak width becomes narrower, which is due to the coatings gradually crystallized. Up to 923.15 K, only the anatase-phase TiO_2 is found. All samples display only the largest characteristic peak of anatase-phase crystal (101 face). It is mainly because that the TiO_2 coating is very thin and the strength of other characteristic peaks is very weak and those peaks do not appear on the figure. The anatase phase is transformed into stable rutile-phase TiO_2 at 973.15 K (2θ = 27.45°) according to JCPDS PDF card 21-1276. In short, the heat treatment temperature of higher than 573.15 K is required to obtain anatase-phase crystalline of the TiO_2 coating. The temperature equaling to or higher than 973.15 K is needed to obtain the thermodynamically stable rutile phase of the TiO_2 coating. The average particle diameter of the TiO_2 nanoparticle coatings annealed at 873.15 K is about 1.69 × 10^{-8} m, which was estimated with the Scherrer equation[40] from the full width at half maximum (FWHM) of the diffraction peak 2θ at 25.28°. Anatase phase has good stability and corrosion protective characteristic on metal.[13]

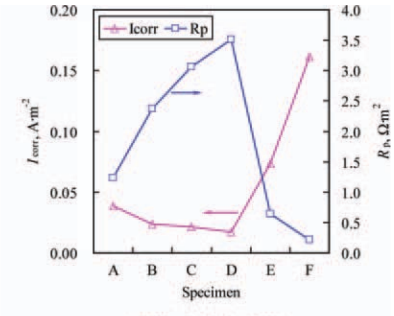

(a) I_{corr} and R_p plots

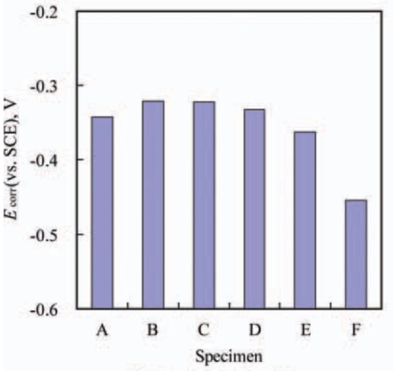

(b) E_{corr} (vs. SCE) plot

Figure 11. I_{corr}, R_p, and E_{corr} (vs. SCE) plots of different samples after the corrosion time of 158 h. (a) I_{corr} and R_p plots; (b) E_{corr} (vs. SCE) plot.

[Color figure can be viewed in the online issue, which is available at wileyonlinelibrary.com.]

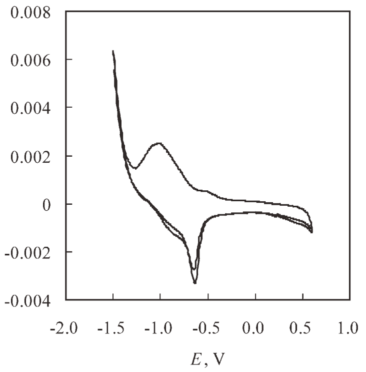

(a) ASS

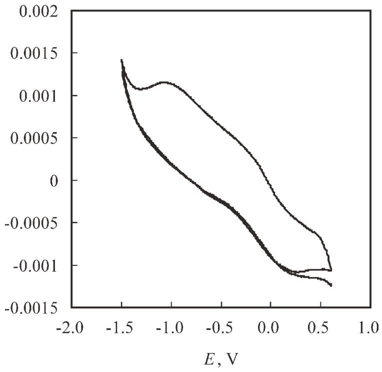

(b) TiO_2 coating

Figure 12. CV curves of the ASS and the TiO_2 coating with thickness of 288.9 ± 0.8 × 10^{-9} m.

(a) ASS; (b) TiO_2 coating.

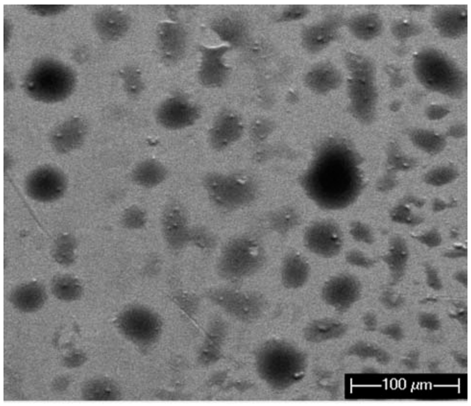

(a) FE-SEM (200X)

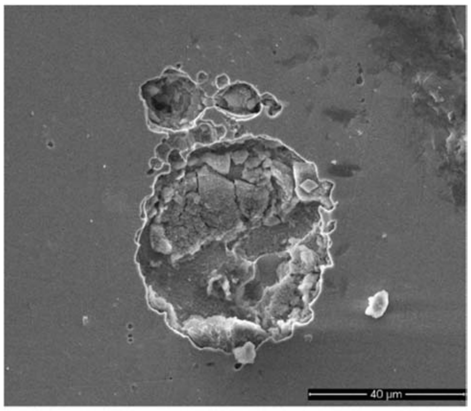

(b) FE-SEM (2000X)

Figure 13. Surface morphology of the pitting corrosion of the ASS substrate in the corrosion media.
(a) ×200; (b) ×2000.

Therefore, the TiO_2 coating with the anatase phase was chosen here as the protective coating layer. The 2θ angles at 43.58, 44.46, 50.68, 64.38, 74.62, and 81.90° shown in Figure 2 are the characteristic diffraction peaks of the ASS substrate.

Morphology and Confirmation of Chemical Elements of TiO_2 Coatings. The morphology of the polished ASS can be observed with the FE-SEM images, as shown in Figure 3. The surface of the polished ASS substrate is very smooth with few sandpaper scratches.

The FE-SEM images (Figures 4–6) reveal that the surface topography of the TiO_2 coating is smooth, crack-free, dense, and uniform. The coating is composed of the accumulation of TiO_2 nanoparticles with diameters of several nanometers. The TiO_2 coatings are transparent and bright. They appear light blue, yellow, blue, purple, yellow green, and green with the increase of deposition time when observed with the naked eyes under natural light.

The thickness of TiO_2 coating increases when prolonging the deposition time. However, the coating with larger thickness is easily ruptured. Figure 7 shows the TiO_2 surface exhibits "muddy cracks" structure. This cracked morphology is due to difference of the thermal expansion coefficients between the TiO_2 coatings and the ASS substrate when they were dried, heated, or cooled in the sintering process.[41,42]

The EDS mapping images confirm the existence of Ti and O elements in the coatings as shown in Figures 4–7. Figures 4–7 show that the TiO_2 coating surfaces become more compact, and the content of Ti element increases with the increase of the deposition time. The mass percentages of Ti (wt. %) are 1.02, 2.93, 4.67, and 6.77%, respectively, and the atom percentages (at. %) are 1.00, 2.67, 4.17, and 5.38%, sequentially. Fe, Cr, Mn, and Ni elements from the ASS substrate are also observed because the depth of electron beam irradiation is several microns, which is far greater than the thickness of TiO_2 coating in EDS analysis. Trace Al and Si elements in the coating surfaces might come from the polishing paste because the polished ASS substrate used for coating preparation might not be completely cleaned. The raw materials of Al and Si elements are Al_2O_3 and SiO_2 compounds, which are the main components of the polishing paste. Trace level of Cu element is also found in Figures 6c and 7c, because the wool polishing wheel was also formerly used to polish copper substrate for other preparation of coatings. The trace copper might have been left into the wool wheel and then entered into the micropores of metal substrates.

Electrochemical corrosion characteristics

PP Curves. PP curves were measured with a scan rate of 1.0×10^{-3} V s^{-1} from -1.50 to 0.60 V. To evaluate the corrosion resistance of the TiO_2 coating, the corrosion potential E_{corr} (vs. SCE) is directly determined on the figure, and the corrosion current density I_{corr} is determined by Tafel's extrapolation method,[43] as shown in Figure 8. Polarization resistance R_p was obtained from E_{corr} (vs. SCE), I_{corr}, and the anodic–cathodic Tafel slopes. The value of polarization resistance R_p was determined from the relationship,[3,13,44]

$$R_p = \frac{\beta_a \beta_c}{2.303 I_{corr}(\beta_a + \beta_c)} \tag{4}$$

Figure 9 shows the scan results of Tafel curves for the TiO_2 coating with thickness of $228.5 \pm 0.9 \times 10^{-9}$ m at different corrosion time. Table 1 lists the electrochemical parameters obtained from the Tafel curves.

Figure 9 shows that the shape of Tafel curves is similar at all corrosion time, which indicates that the corrosion mechanism of the coating has no significant change in the corrosion solution. The results show that E_{corr} shifts toward the negative side from -0.183 to -0.322 V, meanwhile I_{corr} toward the positive side from 0.00272 to 0.0212 A m^{-2} with the increase of the corrosion time as shown in Table 1. The value of R_p at the corrosion time of 158 h is about one sixth of that at 0 h. The results above indicate that the corrosion resistance of the coating deteriorates with the increase of the corrosion time. It is worth mentioning that the coating retained original luster and color although it is corroded for 158 h. However, the corroded ASS surface becomes dull and loses metallic luster.

The Tafel plots obtained for the TiO_2 coatings with different thickness at the corrosion time of 158 h in corrosion solution were also compared with that of the ASS substrate, as shown in Figure 10.

The value of E_{corr} (vs. SCE), I_{corr}, and R_p of the ASS is -0.454 V, 0.161 A m^{-2}, and 0.209 Ω cm^2, respectively. The E_{corr} values of all the coatings shift to positive direction, and the I_{corr} values migrate simultaneously to the smaller corrosion current direction compared with those of the ASS. The potential curves show that the TiO_2 coating inhibits both the cathodic and anodic corrosion processes. It results in the reduction of both the cathodic and anodic current densities

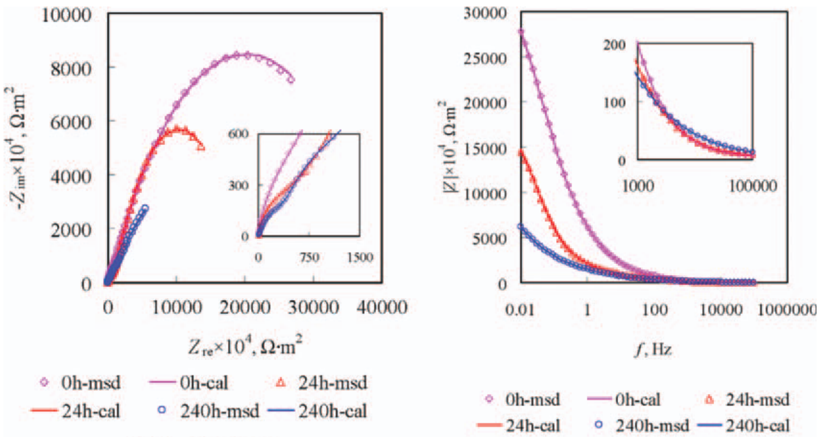

(a) $-Z_{im}$ vs. Z_{re} plot

(b) $|Z|$ vs. f plot

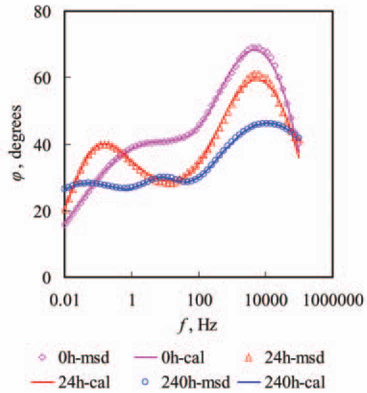

(c) φ vs. f plot

Figure 14. Nyquist and Bode plot of EIS data obtained from the TiO_2 coating with thickness of 228.5 ± 0.9 × 10^{-9} m at different corrosion time (msd, measured data; cal, simulated data).

[Color figure can be viewed in the online issue, which is available at wileyonlinelibrary.com.]

accompanied by the migration of the corrosion potential towards positive values. These results mean that the TiO_2 coatings demonstrate better anticorrosion behavior under the corrosion solution.

Figure 11 shows the corrosion current density, polarization resistance, and corrosion potential plots of different samples after the corrosion time of 158 h. The corrosion current density decreases and the polarization resistance increases with the increase in the coating thickness until the TiO_2 coating thickness is 288.9 ± 0.8 × 10^{-9} m, as shown in Figure 11a. It is probably related to eliminating or decreasing defects of the TiO_2 nanoparticle coating with the increase of deposition time. So, increasing thickness of coating will lead to decreasing of electron transition and rate of electrochemical reactions. The value of R_p decreases sharply when the thickness of the coating increases to 326.5 ± 1.0 × 10^{-9} m. However, the R_p is still higher than that of the ASS, as shown in Figure 11a. According to FE-SEM images as shown in Figure 7, the coating with thickness of 326.5 ± 1.0 × 10^{-9} m is cracked. These coating crevices might cause localized corrosion sites.[3] The densest TiO_2 coating with thickness of 288.9 ± 0.8 × 10^{-9} m has the most noble E_{corr}, the lowest corrosion current I_{corr}, and the highest value of R_p. These values are −0.332 V and 0.017 A m^{-2}, and 3.508 Ω m^2, respectively. Hence, a dense and crack-free coating is available to inhibit the reaction of the corrosion process. Figure 11b shows that corrosion potentials of different coatings vary inconspicuously.

There are two main reasons for the TiO_2 nanoparticle coatings significantly increasing the corrosion resistance compared with the ASS. First, the dense TiO_2 nanoparticles act as inert physical barriers[45] to the pitting corrosion and optimize the nanostructure of the ASS substrate, hence, improve the corrosion resistance of the coating system. Another reason is that the TiO_2 nanoparticles are embedded in the ASS substrate surface layer to generate the interface layer by atomic diffusion in the high-temperature sintering condition. When the corrosion electrolyte diffuses to the interface layer, the TiO_2 coating forms many microgalvanic couples with the ASS substrate that are less noble than the TiO_2 particles.[28,30] So, the TiO_2 coating undergoes strong cathode polarization, which means that any damage or partial removal of the coating does not cause an increased galvanic corrosion of the ASS substrate.

CV Curves. CV is a potential-controlled ‘‘reversal'' electrochemical experiment. A cyclic potential sweep is imposed on an electrode, and the current response is observed. Analysis of the current response can give information about the thermodynamics and kinetics of electron transfer at the electrode–solution interface, as well as the kinetics and mechanisms of solution chemical reactions initiated by the heterogeneous electron transfer.[46]

Figure 12 shows the CV curves of the ASS and the TiO_2 coating. Peak-shaped cyclic voltammograms for the ASS and the TiO_2 coating with thickness of 288.9 ± 0.8 × 10^{-9} m

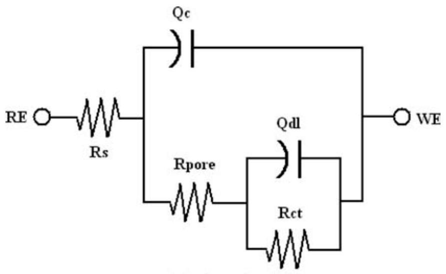

(a) 0h and 24h

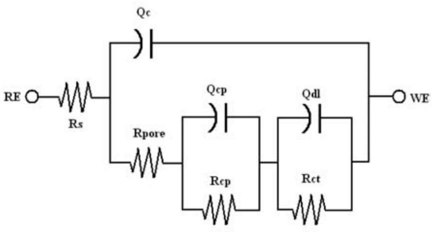

(b) 240h

Figure 15. EC model for the EIS analysis of the TiO_2 coating with thickness of 228.5 ± 0.9 × 10^{-9} m at different corrosion time.

(a) 0 and 24 h; (b) 240 h.

were recorded for two cycles by sweeping the working electrode potential from −1.5 to 0.6 V at a scan rate of 0.05 V s^{-1} in the mixed corrosion solution. All electrode potentials are reported with respect to SCE.

The CV curves for the ASS in the corrosion solution are shown in Figure 12a. The results show that the oxidation peak at potential E_o, −0.63 V, and reduction peak at potential E_r, −1.01 V, are the characteristic peaks of the ASS. This means that the redox reaction on the steel surface occurs during the CV scanning process. However, little corrosion occurs in the TiO_2/ASS system (Figure 12b). By comparison with the scan results, it indicates that the TiO_2 coating has a preservative effect.

In general, the localized corrosion of the ASS in a sodium chloride and hydroxide environment is classified in pitting corrosion, which causes destructive pits in very small surface holes due to the extremely localized anodic reaction sites. Figure 13 shows FE-SEM morphology of the pitting corrosion of the ASS in the mixed corrosion solution. The diameter distribution of the corroded pitting holes is from a few microns to tens of microns. Generally, the ignition of pits occurs at localized sites on a metal surface defects, which may be due to coating failure, mechanical discontinuities, or microstructural phase heterogeneities. In corrosion solution containing chlorine Cl^- and oxygen molecules (O_2), $FeCl_2$ aqueous compound is produced, the initial governing reactions are as follows,[3]

$$Fe \rightleftharpoons Fe^{2+} + 2e^- \tag{5}$$

$$O_2 + 2H_2O + 4e^- \rightleftharpoons 4(OH)^- \tag{6}$$

$$Fe^{2+} + 2Cl^- \rightleftharpoons Fe^{2+}Cl_2^- \tag{7}$$

$$Fe^{2+}Cl_2^- + 2H_2O \rightleftharpoons Fe(OH)_2 + 2H^+Cl^- \tag{8}$$

where H^+Cl^- is the free hydrochloric acid that forms at the bottom of the pits. At the same time, hydroxyl ions, OH^-, in the bulk solution diffuse into the pinholes and react with the hydrogen ions.

$$OH^- + H^+ \rightleftharpoons H_2O \tag{9}$$

Equation 9 promotes the Eq. 8 to the right, which accelerates formation of the metal hydroxide $Fe(OH)_2$ compound. This compound is unstable and reacts further with oxygen and water to form the final corrosion product, iron (III) hydroxide.[3] Hence,

$$2Fe(OH)_2 + 0.5O_2 + H_2O \rightleftharpoons 2Fe(OH)_3 \tag{10}$$

Electrochemical Impedance Spectroscopy. It is well known that EIS testing technique is a powerful tool to investigate the corrosion behavior of the coatings without deterioration of the coating system. To obtain further information about the influence of the corrosion time on the corrosion behavior of the TiO_2 coating, the EIS experiments were carried out at the open-circuit potential (OCP) by applying sinusoidal signal amplitude of ±0.010 V. The electrode response was analyzed in the frequency range from 10^5 to 0.01 Hz.

Figure 14 shows the Nyquist and Bode plots of EIS spectra for the TiO_2 coating with thickness of 228.5 ± 0.9 × 10^{-9} m as the corrosion time increases. The electrical EC with two time constants is used for the corrosion time of 0 and 24 h, which is expressed with the circuit description code (CDC) of R(Q(R(QR))),[5,47] as shown in Figure 15a. This EC is generally used to describe the localized corrosion process of coated metals. The EC with three time constants is used for the EIS test of the TiO_2 coating with the corrosion time of 240 h, and the CDC of R(Q(R(QR)(QR)))[10,48] is shown in Figure 15b. The EIS measurement results are plotted as scattered points, and the simulation data are displayed as fine curves, as shown in Figure 14. The simulation results of the EIS spectra are summarized in Table 2. Good agreement between the simulated and experimental data, as evident from a comparison of the experimental and simulated data, is shown in Figure 16.

One semicircle in the Nyquist plot or one phase angle in the Bode plot generally indicates one time constant of the EIS spectrum as well as corresponds to one parallel circuit in the EC diagram. The smaller semicircle (Figure 14a to the left) in the Nyquist plot or the phase angle in the Bode plots (Figure 14b to the right) at high frequency represents the dielectric characteristic of the TiO_2 coatings.[49] This time constant is expressed with the parallel circuit (Q_c, R_{pore}), in the EC diagram as shown in Figure 15. R_{pore} depends strongly on the conductivity of the electrolyte in the pinholes

Table 2. Optimum Fit Parameters of the TiO_2 Coating with Thickness of 228.5 ± 0.9 × 10^{-9} m at Different Corrosion Time

Corrosion Time (h)	$R_s \times 10^4$ (Ω m^2)	Q_c (Ω^{-1} s^n m^{-2})	n_c	$R_{pore} \times 10^4$ (Ω m^2)	Q_{cp} (Ω^{-1} s^n m^{-2})	n_{cp}	$R_{cp} \times 10^4$ (Ω m^2)	Q_{dl} (Ω^{-1} s^n m^{-2})	n_{dl}	$R_{ct} \times 10^4$ (Ω m^2)
0	4.51	0.0245	0.85	651.1	–	–	–	0.574	0.51	3.93E4
24	4.52	0.0838	0.74	632.2	–	–	–	1.91	0.54	2.92E4
240	4.20	0.266	0.61	414.7	1.46	0.91	297.2	4.45	0.41	2.57E4

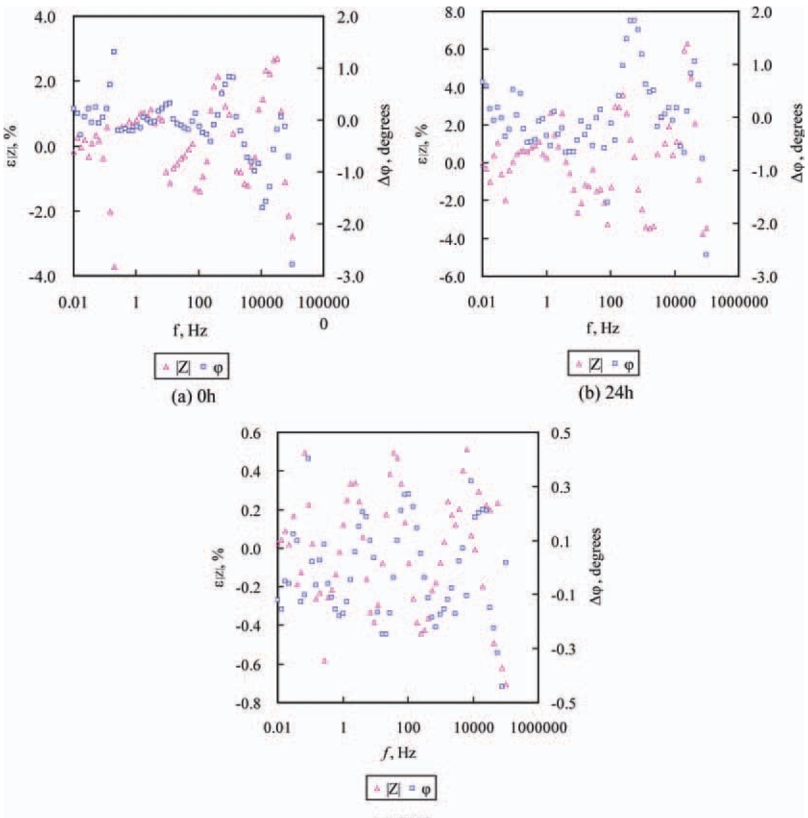

(a) 0h

(b) 24h

(c) 240h

Figure 16. $\varepsilon_{|Z|}$ **and** $\Delta\varphi$ **plots of the** TiO_2 **coating with thickness of** $228.5 \pm 0.9 \times 10^{-9}$ **m at different corrosion time.**

(a) 0 h; (b) 24 h; (c) 240 h. [Color figure can be viewed in the online issue, which is available at wileyonlinelibrary.com.]

of the TiO_2 coating.[50] The schematic diagram of the pinhole and the corrosion model of the ASS substrate are presented in Figure 17. The semicircle at lower frequency in the Nyquist plot is expressed with the parallel subcircuit (Q_{dl}, R_{ct}), which is adopted to describe the charge transfer process at coating/substrate interface at pinholes.[49,51] At the corrosion time of 240 h, the phase angle in the Bode plot at the intermediate frequency might associate with the development of the porous corrosion product layer between the interface of the ASS substrate and the TiO_2 coating. This time constant is expressed with the parallels subcircuit (Q_{cp}, R_{cp}), as shown in Figure 17b.

Figure 14c indicates that the TiO_2 coating has a relatively high-capacitance behavior due to Cl^- in the corrosion solution has not penetrated through the coating in the initial stage of corrosion. The phase angle in the Bode plot is about 70°. With the increase of the corrosion time, the |Z| vs. f plot moves toward the low-frequency direction as well as the phase angle descends, which means that the capacity of the coating reduced gradually. In addition, for the corrosion time of 240 h, the increase of the impedance modulus (frequency-dependent) in the higher frequency range of the |Z| vs. f plot might attribute to a high-corrosion resistance of the corrosion products.[52] As also shown in Table 2, Q_c increases and R_{pore} decreases with the increase of the corrosion time. The results show that the corrosion media has permeated into the substrate through the TiO_2 coating, leading to the formation of localized galvanic cells, which results in the localized corrosion.[53] The Q_{dl} values for the corrosion time of 0, 24, and 240 h are 0.574, 1.91, and 4.45 Ω^{-1} s^n m^{-2}, respectively, which are close to the reported values in the literatures.[48,54–56] R_{ct} decreases gradually and Q_{dl} increases synchronously with the increase of the corrosion time. The value of R_s remains substantially unchanged, which indicates that three-electrode electrochemical test system is relatively stable. However, it is well known that the EIS test is sensitive to many factors and it is difficult, or even impossible to interpret all detailed features of the EIS spectra.[50]

The corrosion model of the TiO_2 coating with different corrosion time is shown in Figure 17. To validate the proposed model, the surface morphology of the TiO_2 coating with thickness of $228.5 \pm 0.9 \times 10^{-9}$ m which has been corroded for 240 h in the corrosion solution as shown in Figure 18. It is found that the multistage corrosion[36] process of the TiO_2 coating might have happened. First, the corrosion media permeates through the pinholes of the TiO_2 coating and then arrive at the stainless steel substrate, so the substrate is corroded and hollowed out. With the increase in the corrosion time, more electrolytes are accessible to the bare stainless steel and accelerate further corrosion. Finally, the coating around the pinholes might rupture and split off from the ASS substrate. So, the pinholes become larger and larger.

Concluding Remarks

The FE-SEM results show that the surface topography of the TiO_2 coating is smooth, crack-free, dense, and uniform. The coating is composed of the accumulation of particles with a few tens of nanometers. The EDS analyses show that the TiO_2 coating surfaces become more compact and the content of Ti element increases with the increase of deposition time. The XRD results show that the anatase-phase structure coatings are available when the sintering temperature is between 673.15 and 923.15 K. The peak intensity of anatase phase increases and the peak width becomes narrower with the increase of the calcined temperature.

The PP and two circles of the CV scanning tests both show that the coatings demonstrate better anticorrosion behavior compared with the ASS substrate. The corrosion current density decreases and the polarization resistance increases in PP with the increase of the coating thickness until the thickness reaches to $288.9 \pm 0.8 \times 10^{-9}$ m. The corrosion resistance of the TiO_2 coatings deteriorates with the increase of the corrosion time. The anticorrosion performance of the TiO_2 coating is due to two aspects: first, the dense, compact TiO_2 nanoparticles act as the inert physical barriers to prohibit the pitting corrosion and optimize the nanostructure of the ASS substrate; second, the TiO_2 nanoparticles are embedded in the ASS substrate surface layer to generate the interface layer by atomic diffusion in the high-temperature sintering condition. When the corrosion electrolyte diffuses to the interface layer, the TiO_2 coating undergoes strong cathode polarization, which means that any damage or partial removal of the coating does not cause an increased galvanic corrosion of the ASS substrate.

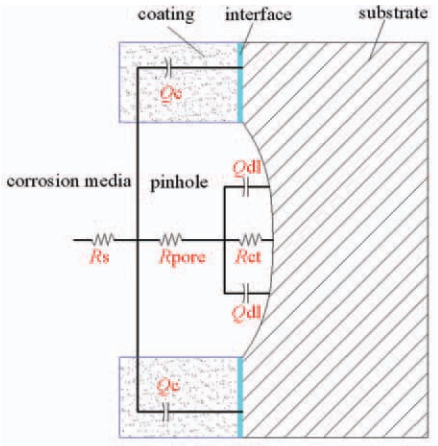

(a) 0 and 24h

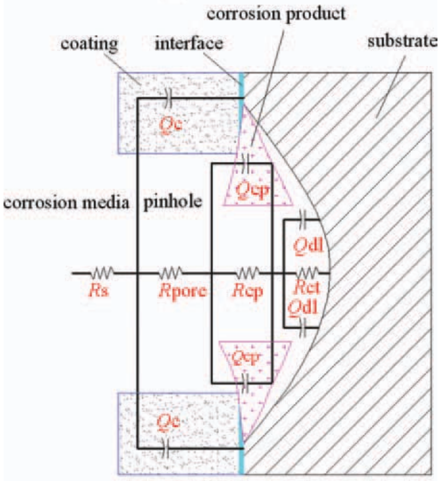

(b) 240h

Figure 17. The schematic diagram of the pinhole and the corrosion model of the ASS substrate.

(a) 0 and 24 h; (b) 240 h. [Color figure can be viewed in the online issue, which is available at wileyonlinelibrary.com.]

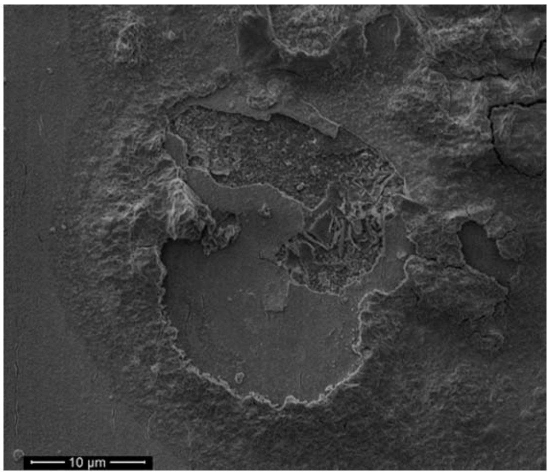

Figure 18. Surface morphology of the TiO_2 coating with thickness of $228.5 \pm 0.9 \times 10^{-9}$ m after the corrosion time of 240 h.

The EIS tests indicate that the TiO_2 coating has a relatively high-capacitance behavior in the initial stage of corrosion process. The capacity of the TiO_2 coating has reduced slightly, and the corrosion electrolyte has penetrated to the ASS substrate through the pinholes and led to the localized corrosion with the increase of the corrosion time. The capacitance and the resistance of the corrosion product layer between the interface of the ASS substrate and the TiO_2 coating are found after the corrosion time of 240 h. The surface morphology of the TiO_2 coating after corrosion both show that the multistage corrosion process might have happened. Because the TiO_2 nanoparticles coating has a conspicuous corrosion resistance, further work will focus on the heat transfer and the antifouling performance of the coating on the ASS in the pool boiling conditions.

Acknowledgments

The authors are grateful to the National Natural Science Foundation of China (grant numbers: 20876106) and Tianjin Research Program of Application Foundation and Advanced Technology (no. 09JCZDJC24100) for the financial support. The authors also wish to thank Professor Jixiao Wang for his kindly help in the electrochemical studies.

Notation

DI = diffraction intensity of X-ray/counts
E_{corr} = corrosion potential, V
E_o = potential of oxidation peak, V
E_r = potential of reduction peak, V
f = frequency, Hz
I_{corr} = corrosion current density, A m^{-2}
l_r = sampling length, m
n = empirical exponent between 0 and 1
Q_c = capacitance at the solution/coating interface, Ω^{-1} s^n m^{-2}
Q_{cp} = capacitance properties of the corrosion layer, Ω^{-1} s^n m^{-2}
Q_{dl} = capacitance at the solution/substrate interface, Ω^{-1} s^n m^{-2}
R_a = arithmetical mean deviation, m
R_{cp} = resistance properties of the interface layer, Ω m^2
R_{ct} = charge transfer resistance at the solution/substrate interface, Ω m^2
R_p = polarization resistance, Ω m^2
R_{pore} = resistance resulted from the coating pores, channels or cracks, Ω m^2
R_q = root mean square deviation, m
R_s = resistance of the electrolyte between working electrode and reference electrode, Ω m^2
R_z = the maximum height of profile, m

Y_0 = admittance constant
Z = impedance in Nyquist plot, $\Omega\ m^2$
Z_{im} = imaginary part of impedance of EIS, $\Omega\ m^2$
Z_{re} = real part of impedance of EIS, $\Omega\ m^2$
$|Z|$ = modulus of Z, $\Omega\ m^2$

Greek letters

β_a = anodic polarization constant or Tafel anodic slope, V dec^{-1}
β_c = cathodic polarization constant or Tafel cathodic slope, V dec^{-1}
θ = Bragg X-ray diffraction angle of the crystal, °
φ = phase angle in Bode plot, °
ω = angle frequency, Hz
$\varepsilon_{|Z|}$ = relative fitting errors of |Z|, %
$\Delta\varphi$ = deviation of φ, °

Abbreviations

AFM = atomic force microscopy
ASS = AISI304 stainless steel
CDC = circuit description code
CPE = constant phase element
CV = cyclic voltammetry
CVD = chemical vapor deposition
EC = equivalent circuit
EDS = energy-dispersive X-ray spectroscopy
EIS = electrochemical impedance spectroscopy
FE-SEM = field emission scanning electron microscopy
FWHM = full width at half maximum
LPD = liquid-phase deposition
OCP = open-circuit potential
PP = potentiodynamic polarization
RE = reference electrode
SAM = self-assembled monolayer
SCE = saturated calomel electrode
WE = working electrode
XRD = X-ray diffraction

Literature Cited

1. Somerscales EFC, Kassemi M. Fouling due to corrosion products formed on a heat transfer surface. *J Heat Trans*. 1987;109:267–271.
2. Somerscales EFC. Fundamentals of corrosion fouling. *Exp Therm Fluid Sci*. 1997;14:335–355.
3. Perez N. *Electrochemistry and Corrosion Science*. Boston: Kluwer Academic Publishers, 2004.
4. Maier B, Frankel GS. Pitting corrosion of bare stainless steel 304 under chloride solution droplets. *J Electrochem Soc*. 2010;157: C302–C312.
5. Padhy N, Kamal S, Chandra R, Kamachi Mudali U, Raj B. Corrosion performance of TiO_2 coated type 304L stainless steel in nitric acid medium. *Surf Coat Technol*. 2010;204:2782–2788.
6. Glö*β* D, Frach P, Zywitzki O, Modes T, Klinkenberg S, Gottfried C. Photocatalytic titanium dioxide thin films prepared by reactive pulse magnetron sputtering at low temperature. *Surf Coat Technol*. 2005;200:967–971.
7. Liu MY, Wang H, Wang Y. Enhancing flow boiling and antifouling with nanometer titanium dioxide coating surfaces. *AIChE J*. 2007; 53:1075–1085.
8. Wang Y, Wang LL, Liu MY. Antifouling and enhancing pool boiling by TiO_2 coating surface in nanometer scale thickness. *AIChE J*. 2007;53:3062–3076.
9. Wang LL, Liu MY. Pool boiling fouling and corrosion properties on liquid-phase-deposition TiO_2 coatings with copper substrate. *AIChE J*. 2011;57:1710–1718.
10. Szalkowska E, Gluszek J, Masalski J, Tylus W. Structure and protective properties of TiO_2 coatings obtained using the sol–gel technique. *J Mater Sci Lett*. 2001;20:495–497.
11. Shen GX, Chen YC, Lin CJ. Corrosion protection of 316 L stainless steel by a TiO_2 nanoparticle coating prepared by sol–gel method. *Thin Solid Films*. 2005;489:130–136.
12. Shanaghi A, Sabour Rouhaghdam A, Shahrabi T, Aliofkhazraei M. Study of TiO_2 nanoparticle coatings by the sol–gel method for corrosion protection. *Mater Sci*. 2008;44:233–247.
13. Shanaghi A, Sabour AR, Shahrabi T, Aliofkhazraee M. Corrosion protection of mild steel by applying TiO_2 nanoparticle coating via sol–gel method. *Prot Met Phys Chem Surf*. 2009;45:305–311.
14. Bendavid A, Martin PJ, Preston EW. The effect of pulsed direct current substrate bias on the properties of titanium dioxide thin films deposited by filtered cathodic vacuum arc deposition. *Thin Solid Films*. 2008;517:494–499.
15. Rausch N, Burte EP. Thin TiO_2 films prepared by low pressure chemical vapor deposition. *J Electrochem Soc*. 1993;140: 146–149.
16. Ahn KH, Park YB, Park DW. Kinetic and mechanistic study on the chemical vapor deposition of titanium dioxide thin films by in situ FT-IR using TTIP. *Surf Coat Technol*. 2002;171:198–204.
17. Masuda Y, Sugiyama T, Lin H, Seo WS, Koumoto K. Selective deposition and micropatterning of titanium dioxide thin film on self-assembled monolayers. *Thin Solid Films*. 2001;382:153–157.
18. Zoppi RA, Trasferetti BC, Davanzo CU. Sol–gel titanium dioxide thin films on platinum substrates: preparation and characterization. *J Electroanal Chem*. 2003;544:47–57.
19. Zeng ZO, Xiao ZW, Zhao GP. Titanium dioxide coating prepared on 304 stainless steel by liquid phase deposition method. *J Electroplating Finishing (China)*. 2008;27:45–51.
20. Deki S, Aoi Y, Hiroi O, Kajinami A. Titanium (IV) oxide thin films prepared from aqueous solution. *Chem Lett*. 1996;25:433–434.
21. Nagayama H, Honda H, Kawahara H. A new process for silica coating. *J Electrochem Soc*. 1988;135:2013–2016.
22. Yu JG, Yu HG, Cheng B, Zhao XJ, Yu JC, Ho WK. The effect of calcination temperature on the surface microstructure and photocatalytic activity of TiO_2 thin films prepared by liquid phase deposition. *J Phys Chem B*. 2003;107:13871–13879.
23. Pourmand M, Taghavinia N. TiO_2 nanostructured films on mica using liquid phase deposition. *Mater Chem Phys*. 2008;107: 449–455.
24. Herbig B, Löbmann P. TiO_2 photocatalysts deposited on fiber substrates by liquid phase deposition. *J Photochem Photobiol A*. 2004; 163:359–365.
25. Hu J, Shaokang G, Zhang C, Ren C, Wen C, Zeng Z, Peng L. Corrosion protection of AZ31 magnesium alloy by a TiO_2 coating prepared by LPD method. *Surf Coat Technol*. 2009;203: 2017–2020.
26. Yuan JN, Tsujikawa S. Charaterization of sol–gel-derived TiO_2 coatings and their photoeffects on copper substrates. *J Electrochem Soc*. 1995;142:3444–3450.
27. Ovenstone J, Yanagisawa K. Effect of hydrothermal treatment of amorphous titania on the phase change from anatase to rutile during calcination. *Chem Mater*. 1999;11:2770–2774.
28. Głuzek J, Masalski J, Furman P, Nitsch K. Structural and electrochemical examinations of PACVD TiO_2 films in Ringer solution. *Biomaterials*. 1997;18:789–794.
29. Xiao QF. *Preparation of TiO_2 Films by Electrochemical Deposition Method and its Anticorrosion Performance Study*. Zhengzhou, China: Zhengzhou University, 2007.
30. Baghery P, Farzam M, Mousavi AB, Hosseini M. Ni–TiO_2 nanocomposite coating with high resistance to corrosion and wear. *Surf Coat Technol*. 2010;204:3804–3810.
31. Schmitt RH, Grove EL, Brown RD. The equivalent conductance of the hexafluorocomplexes of group IV (Si, Ge, Sn, Ti, Zr, Hf). *J Am Chem Soc*. 1960;82:5292–5295.
32. Wamser CA. Equilibria in the system boron trifluoride–water at 25 °C. *J Am Chem Soc*. 1951;73:409–416.
33. Deki S, Aoi Y, Asaoka Y, Kajinami A, Mizuhata M. Monitoring the growth of titanium oxide thin films by the liquid-phase deposition method with a quartz crystal microbalance. *J Mater Chem*. 1997;7:733–736.
34. http://www.new-span.com/products/optinstr/thinfilm.php.
35. International Organization for Standardization. Geometrical product specifications (GPS)-surface texture: profile method-terms, definitions and surface texture parameter, 1997. ISO 4287–1997.
36. Li M, Luo S, Zeng C, Shen J, Lin H, Cao C. Corrosion behavior of TiN coated type 316 stainless steel in simulated PEMFC environments. *Corros Sci*. 2004;46:1369–1380.
37. Loveday D, Peterson P, Rodgers B. Evaluation of organic coatings with electrochemical impedance spectroscopy. Part 3: Protocols for testing coatings with EIS. *J Coat Technol*. 2005;2:22–27.
38. Liu C, Bi Q, Leyland A, Matthews A. An electrochemical impedance spectroscopy study of the corrosion behavior of PVD coated steels in 0.5 N NaCl aqueous solution: Part I. Establishment of equivalent circuits for EIS data modeling. *Corros Sci*. 2003;45: 1243–1256.

39. Aziz-Kerrzo M, Conroy KG, Fenelon AM, Farrell ST, Breslin CB. Electrochemical studies on the stability and corrosion resistance of titanium-based implant materials. *Biomaterials*. 2001;22:1531–1539.
40. Patterson AL. The Scherrer formula for X-ray particle size determination. *Phys Rev*. 1939;56:978–982.
41. Ma B, Goh GKL, Ma J, White TJ. Growth kinetics and cracking of liquid-phase-deposited anatase films. *J Electrochem Soc*. 2007;154: D557–D561.
42. Yamabi S, Imai H. Crystal phase control for titanium dioxide films by direct deposition in aqueous solutions. *Chem Mater*. 2002;14: 609–614.
43. Depenyou FJ, Doubla A, Laminsi S, Moussa D, Brisset JL, Le Breton JM. Corrosion resistance of AISI 1018 carbon steel in NaCl solution by plasma–chemical formation of a barrier layer. *Corros Sci*. 2008;50:1422–1432.
44. Stern M, Geary AL. Electrochemical polarization I. A theoretical analysis of the shape of polarization curve. *J Electrochem Soc*. 1957;104:56–63.
45. Chen XH, Chen CS, Xiao HN, Cheng FQ, Zhang G, Yi GJ. Corrosion behavior of carbon nanotubes–Ni composite coating. *Surf Coat Technol*. 2005;191:351–356.
46. Gosser DK. *Cyclic voltammetry: simulation and analysis of reaction mechanisms*. New York: VCH Publishers, Inc., 1993.
47. Pan J, Thierry D, Leygraf C. Electrochemical impedance spectroscopy study of the passive oxide film on titanium for implant application. *Electrochim Acta*. 1996;41:1143–1153.
48. Cheng YL, Zhang Z, Cao FH, Li JF, Zhang JQ, Wang JM, Cao CN. A study of the corrosion of aluminum alloy 2024-T3 under thin electrolyte layers. *Corros Sci*. 2004;46:1649–1667.
49. Liu C, Bi Q, Matthews A. EIS comparison on corrosion performance of PVD TiN and CrN coated mild steel in 0.5 N NaCl aqueous solution. *Corros Sci*. 2001;43:1953–1961.
50. Pan J, Leygraf C, Jargelius-Pettersson RFA, Lindén J. Characterization of high-temperature oxide films on stainless steels by electrochemical-impedance spectroscopy. *Oxid Met*. 1998;50:431–455.
51. Loveday D, Peterson P, Rodgers B. Evaluation of organic coatings with electrochemical impedance spectroscopy. Part 2: Application of EIS to coatings. *J Coat Technol*. 2004;1:88–93.
52. Rosborg B, Pan JS. An electrochemical impedance spectroscopy study of copper in a bentonite/saline groundwater environment. *Electrochim Acta*. 2008;53:7556–7564.
53. William Grips VK, Barshilia HC, Selvi VE, Kalavati, Rajam KS. Electrochemical behavior of single layer CrN, TiN, TiAlN coatings and nanolayered TiAlN/CrN multilayer coatings prepared by reactive direct current magnetron sputtering. *Thin Solid Films*. 2006;514:204–211.
54. Castro EB, Gervasi CA. Electrodeposited Ni–Co-oxide electrodes: characterization and kinetics of the oxygen evolution reaction. *Int J Hydrogen Energy*. 2000;25:1163–1170.
55. Rahsepar M, Bahrololoom ME. Corrosion study of Ni/Zn compositionally modulated multilayer coatings using electrochemical impedance spectroscopy. *Corros Sci*. 2009;51:2537–2543.
56. Lin CH, Duh JG. Electrochemical impedance spectroscopy (EIS) study on corrosion performance of CrAlSiN coated steels in 3.5 wt. % NaCl solution. *Surf Coat Technol*. 2009;204:784–787.

Manuscript received Dec. 29, 2010, and revision received May 3, 2011.